Experiments with DGSEM Shock-capturing Schemes

Scott M. Murman, Nicholas K. Burgess,* Laslo T. Diosady*, and
Anirban Garai*

NASA Ames Research Center, Moffett Field, CA, USA

Abstract

Three shock-capturing formulations for an entropy-stable discontinuous-Galerkin spectral-element solver are examined: Galeão and Dutra do Carmo's cross-wind stabilization, Barter and Darmofal's differential equation for propagating and diffusing the artificial viscosity, and a novel method based on inter-element jumps of pressure and a modified Ducros-style sensor. The behavior of the schemes is evaluated using standard inviscid and viscous test cases for shock-capturing methods, along with homogeneous isotropic turbulence, to assess the robustness and accuracy of the methods. The novel artificial viscosity scheme provides a straightforward and robust shock-capturing method for the current fluid solver that does not dampen turbulent fluctuations.

1 Introduction

One of the pacing items for the mainstream adoption of unstructured high-order methods is the development of a robust and general shock-capturing scheme that is competitive with the total variation diminishing (TVD) schemes commonly used in 2nd-order finite-volume formulations, without sacrificing the improved accuracy and efficiency of high-order methods. During the last several years, we have been developing a discontinuous-Galerkin spectral-element method (DGSEM) for scale-resolving simulations[1–6]. While this approach

---

*Science and Technology Corp.

This material is declared a work of the U.S. Government and is not subject to copyright protection in the United States.

American Institute of Aeronautics and Astronautics

has shown the promise of improvement over low-order methods for scale-resolving simulations, while still maintaining the geometric flexibility of unstructured meshing, all of the validation examples consider low-speed applications due to the lack of an aforementioned shock-capturing scheme. The goal of this work is to analyze, and ultimately develop, a new shock-capturing methodology for the DGSEM framework, with a focus on shock-turbulence interaction.

There are several established shock-capturing methods for DG schemes that have been demonstrated for steady-state simulations. One common approach is to develop a shock sensor, and reduce the polynomial order of the solution space in the region surrounding the shock, while simultaneously increasing the resolution, *i.e.* feature-based *h-p* adaptation[7, 8]. In the context of a multiscale approach to sub-grid turbulence modeling, this approach effectively eliminates any turbulence from the shock region, which is obviously undesirable. A more sophisticated approach is to use the multiple scales inherent in high-order simulations to develop a spectral sensor, which is then combined with an artificial viscosity model, to suppress oscillations in the shock region[9, 10]. This approach has been demonstrated for unsteady problems, however for scale-resolving turbulent simulations the spectral sensor will be active uniformly in space until all scales are fully resolved, so the approach effectively becomes a Smagorinsky-like closure model which corrupts more sophisticated sub-grid models.

An alternative approach by Barter and Darmofal[11] takes advantage of the discontinuous nature of the pressure field between elements to develop a shock sensor which does not examine the spectral scale separation, making it more attractive (on paper) for scale-resolving simulations. This sensor is used as the source term in an auxiliary differential equation to provide a smooth variation of the artificial viscosity coefficient (*cf.* [11, 12]). This approach has been successfully applied to viscous blunt body flows through Mach 17[13, 14].

Lastly, methods which incorporate the strong form of the residual operator to construct a so-called cross-wind diffusion operator have been tested[15–17]. These schemes are attractive, as they start from a more mathematical point of view, however there is limited practical experience in the literature on their application for spectral-element DG schemes.

The current paper examines the cross-wind diffusion operator, Barter and Darmofal's shock-capturing differential equation, as well as a novel shock-capturing formulation to better understand the performance attributes of these schemes in our DGSEM solver. Benchmark test cases for shock-capturing and turbulent flows are considered. The paper begins with a brief review of the pertinent details of the DGSEM solver before examining the shock-

American Institute of Aeronautics and Astronautics

capturing schemes.

2   Numerical Solver

The current work focuses on an entropy-stable DG spectral-element scheme, which supports arbitrary order in space and time. All of the computations in the current work use the inviscid Riemann flux of Ismail and Roe[18] and a viscous stabilization similar to the second scheme of Bassi and Rebay[19]. No specific corrections for the shock carbuncle problem are applied.

The numerical scheme is designed specifically for scale-resolving simulations using a multiscale approach. Of particular note for the current work is the use of a tensor-product preconditioner based on an approximate factorization of the inviscid flux Jacobian across a finite element[20]. This provides an efficient scalar preconditioner for an advection-type equation, which is competitive with block-diagonal approaches, while requiring a fraction of the memory and algorithmic complexity. The downside of this is the inability to condition significant diffusion terms or cross-coupled source terms. In developing high-order shock-capturing schemes these can be significant liabilities, and part of the motivation for the current work is investigating the seriousness of the problem, and possible mitigation strategies.

3   Cross-wind Stabilization

We start by exploring Galeão and Dutra do Carmo's cross-wind stabilization[15] in our entropy-stable DGSEM scheme.[*] This adds artificial viscosity to the system of equations using a dissipative volume operator based on a quadratic of the strong form of the residual,

$$D_{cw} = \frac{(\mathcal{L}v)^T \tau (\mathcal{L}v)}{(\nabla v)^T \tilde{A}_0 (\nabla v)} \tag{1}$$

where v are the entropy variables, $\tilde{A}_0$ is the metric tensor for the entropy variables, and $\mathcal{L}$ is the nonlinear operator for the entire system. This acts only in the direction of the solution gradient.

The scheme was applied to the viscous Burgers equation with sinusoidal initial conditions using an 8th-order polynomial basis (Fig. 1). The shock-capturing operator does not com-

---

[*]Barth[16] and Hildebrand and Mishra[17] utilize a similar operator.

American Institute of Aeronautics and Astronautics

pletely suppress non-positive overshoots around the shock, and the artificial viscosity is very noisy, inhibiting the convergence of the system. Note that positivity of density and temperature is a prerequisite for entropy-stability of the Navier-Stokes equations, not a consequence, so that while the non-positive overshoots are not fatal for Burgers equation, they are a significant problem. Arbitrarily scaling the shock-capturing operator by small values (2-5x) does smooth the solution, but still does not completely suppress the non-positive overshoots, and becomes too stiff to converge at even modest scalings. As the operator greatly increases the stiffness of the system, requires a strong-form of the residual which negates many of the benefits of a discontinuous-Galerkin formulation, and requires an arbitrary scaling for practical effectiveness, this approach was not pursued further.
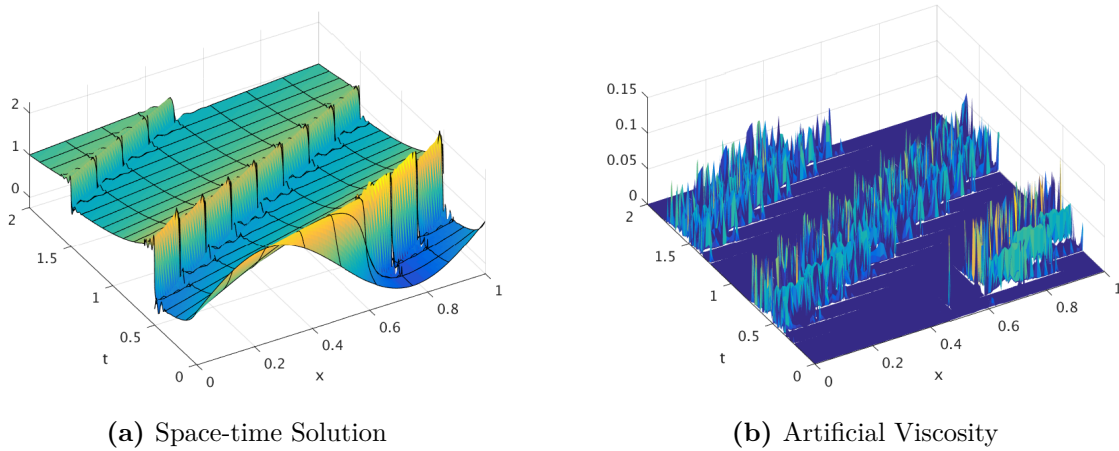

(a) Space-time Solution   **(b)** Artificial Viscosity

Figure 1: Space-time solution of viscous Burgers equation using Galeão and Dutra do Carmo's artificial viscosity scheme.

4   Artificial Diffusion

There are numerous *ad-hoc* methods to add an "artificial" viscosity to the Navier-Stokes equations to suppress undesirable oscillations. One common and effective method uses an artificial diffusion coefficient with a Laplacian operator of the flow variables. The crosswind stabilization from the previous section is an example. In the current effort, we are concerned specifically with turbulence scale-resolving methods. As the Laplacian approach does not have a clear physical analogue in compressible flows, it is difficult to incorporate with subgrid-scale models for LES, and is not preferred here.

Following the physical diffusion in the Navier-Stokes equations, $\tau_{ij} = \mu \left(u_{i,j} + u_{j,i} \right) +$

$\lambda u_{k,k} \delta_{ij}$, artificial viscosity can be created which mimics either the shear (μ) or bulk viscosity (λ) coefficients, typically using an analogous Prandtl number to dissipate the energy equation. Artificial dissipation is not added to the mass balance in this approach. Choosing an artificial bulk viscosity does not dissipate vorticity (*cf.* Mani *et al.* [21]), however it does directly damp acoustic perturbations, while the opposite is true if the shear velocity is chosen. Further, the mechanical pressure in a fluid ($\tilde{p}$) is given by

$$\tilde{p} = p + \left(\lambda + \frac{2}{3}\mu \right) u_{k,k} \tag{2}$$

Stokes' hypothesis thus ensures that the mechanical and thermodynamic pressure are identical. If the artificial viscosity scheme does not also satisfy Stokes' hypothesis, this is no longer the case, and the resulting scheme may not correctly predict the Rankine-Hugoniot jump conditions[22].

The numerical experiments using the current shock capturing schemes empirically demonstrate that specifying the shear artificial viscosity and having the bulk artificial viscosity follow by Stokes' hypothesis is more robust than specifying a bulk viscosity alone.

5   Barter and Darmofal Shock-capturing Method

Barter and Darmofal's shock-capturing method[11] is presented for completeness and as an introduction to the modifications which follow. The scheme uses an auxiliary differential equation

$$\epsilon_{,t} - \left(\frac{L^2}{\tau} \epsilon_{,j} \right)_{,j} = \frac{1}{\tau} \left(\lambda h S - \epsilon \right) \tag{3}$$

which acts as an unsteady differential equation to diffuse the shock capturing working variable ϵ. The variables τ is a timescale, L and h are length scales, λ is a velocity scale, and S is a source term which controls the growth or decay of the working variable. These scales and the source term depend upon the flow state, and are hence coupled to the flow equations. The artificial viscosity is then constructed from ϵ using a nonlinear filter,

$$\mu_s = \begin{cases} 0 & \text{if} \quad \epsilon \leq \epsilon_{min} \\ \epsilon_{max} & \text{if} \quad \epsilon \geq \epsilon_{max} \\ \frac{\epsilon_{max}}{2} \left[1 + \sin \left(\pi \Delta \epsilon \right) \right] & \text{if} \quad \epsilon_{min} < \epsilon < \epsilon_{max} \end{cases} \tag{4}$$

American Institute of Aeronautics and Astronautics

where $\epsilon_{min} = 0.01\lambda\bar{h}$, $\epsilon_{max} = \lambda\bar{h}$, and $\Delta\epsilon = \frac{\epsilon - \epsilon_{min}}{\epsilon_{max} - \epsilon min} - \frac{1}{2}$.

By construction, the auxiliary differential equation diffuses artificial viscosity generated by the source term. The source term is based on a pressure jump indicator,[*]

$$J_\kappa = \frac{1}{|\partial\kappa|} \int_{\partial\kappa} \left| \frac{[\![p]\!]}{\{p\}} \right| \cdot \boldsymbol{n} dS \tag{5}$$

which is integrated over all faces of an element. This converges as

$$J_\kappa = \begin{cases} \mathcal{O}\left(h^{p+1}\right), & \text{smooth} \\ \mathcal{O}\left(1\right), & \text{discontinuity} \end{cases} \tag{6}$$

depending upon whether the flow contains singularities such as strong shocks. The shock sensor is constructed from the pressure jump indicator as

$$S = \begin{cases} 0 & \text{if} \quad \log_{10}\left(J_\kappa\right) \le \psi_{min} \\ 1 & \text{if} \quad \log_{10}\left(J_\kappa\right) \ge \psi_{max} \\ \frac{1}{2}\left[1 + \sin\left(\pi\Delta\psi\right)\right] & \text{if} \quad \psi_{min} < \log_{10}\left(J_\kappa\right) < \psi_{max} \end{cases} \tag{7}$$

where $\psi_{min} = -2 - \log_{10}(p+1)$, $\psi_{max} = -1 - \log_{10}(p+1)$, and $\Delta\psi = \log_{10}\left(J_\kappa\right) + 1.5 + \log_{10}(p+1)$.

The above model is tested with the DG spectral-element solver by computing the flow over an RAE 2822 airfoil at Mach=0.925, $\alpha = 2.92°$, $Re = 60$k, using 4th-order in space and time. A snapshot from this unsteady simulation is provided in Fig. 2. The computed Mach number field shows that the flow separates from the suction side of the airfoil at roughly the 3/4-chord location, and a shock forms near the trailing edge. Figure 2b contains the distribution of the working variable ϵ. As expected, the variation of ϵ is smooth, and does recognize the shock location near the trailing edge, however some issues are apparent. The largest magnitude of viscosity occurs during the expansion of the flow around the leading edge, which is clearly unnecessary in terms of suppressing oscillations across a shock. This occurs because the shock sensor is not able to discern expansion from compression, and the large value of the diffusion coefficient in the shock-capturing model allows this viscosity to spread across, and corrupt, many elements near the leading edge. This smoothing was the intention of the original model, however it has a deleterious effect in turbulent flow

[*]Krivodonova *et al.* [23] utilize a similar jump sensor.

American Institute of Aeronautics and Astronautics

simulations. The effect of diffusion on the convergence of the system will be discussed further subsequently.
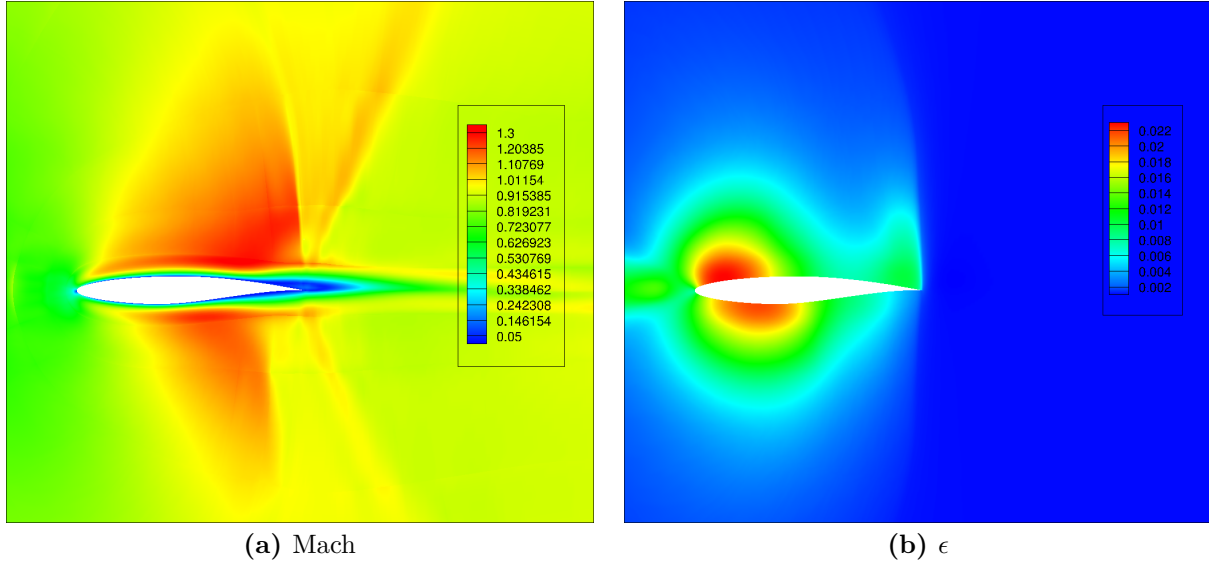

(a) Mach

(b) ϵ

Figure 2: Snapshot from the unsteady simulation of flow over an RAE 2822 airfoil ($Ma = 0.925$, $\alpha = 2.92°$, $Re = 60$k).

The second test case considers the decay of homogeneous isotropic turbulence (HIT) at an initially high turbulent mach number, $Ma_t = \frac{\sqrt{2k}}{3} = 0.6$ using 8th-order in space and time and 32^3 degrees of freedom. The HIT is initially generated to a stationary state at $Re_\lambda = 45$ using the linear forcing methodology described in Garai *et al.* [6], then the forcing is removed and the turbulence decays. Figure 3 presents a snapshot of the Mach number and the artificial bulk viscosity from a slice through the domain during the decay. The artificial viscosity is normalized by the molecular viscosity coefficient. There is a reasonable correlation between high-speed regions and areas of large artificial viscosity, however the entire domain is being overly dissipated even though the flowfield only contains regions of smooth compression and weak shocklets. The shock sensor misinterprets the under-resolved turbulence as discontinuities. If any region strongly triggers the shock sensor, every element in the domain becomes influenced due to the large diffusion coefficient in Eqn. 3.

The influence of the artificial viscosity on the turbulence statistics in inferred in Fig. 4 using the variation of the kinetic energy and the pressure-dilatation correlation ($\int pu_{k,k}$). The behavior of the shock-capturing scheme is compared to an implicit LES/under-resolved DNS simulation, which remains stable at these conditions. The Barter model dissipates the kinetic energy in the domain more strongly than the base entropy-stable scheme and does

American Institute of Aeronautics and Astronautics

not contain any oscillations due to the acoustic energy. In this simulation a bulk artificial viscosity is used, as discussed above, and from Fig. 4b we see that the pressure dilatation term is nearly completely removed at these coarse resolutions. Note that the strongly oscillatory behavior of the pressure-dilatation correlation is an acoustic response to the perturbation in initial conditions, not a spurious result. Lastly, the shock-capturing simulations require roughly 1000x the computational effort as the base scheme due to the increased stiffness of the system.

(a) Mach number   **(b)** Artificial Viscosity
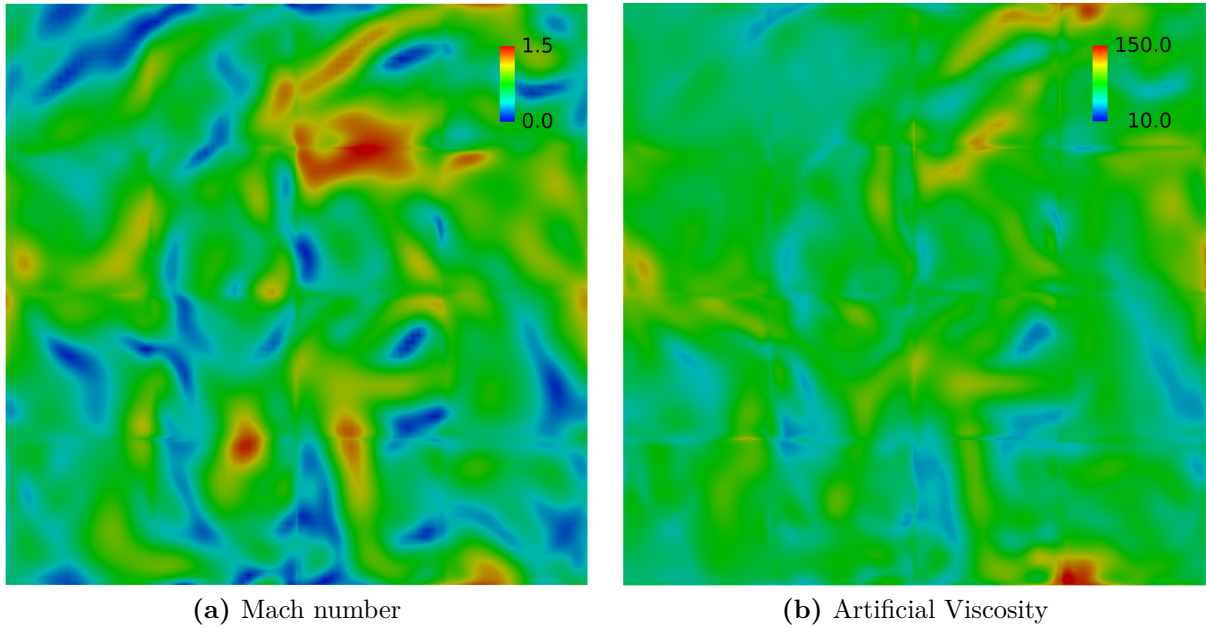
Figure 3: A snapshot through the domain during the decay of homogeneous isotropic turbulence ($Re_\lambda = 45$, $Ma_t = 0.6$).

The diffusion coefficient in Barter and Darmofal's model, $\frac{L^2}{\tau}$, reduces to $15\lambda h$ scaled by a mesh anisotropy diagonal matrix. As $Re = \frac{\lambda h}{\nu} \gg 1$, this means that the artificial viscosity equation has a diffusion that is orders of magnitude larger than the physical diffusion of the fluid equations, leading to a very stiff system which is dominated by convection in the flow equations and diffusion in the auxiliary equation. The current DGSEM fluid solver leverages a tensor-product sum-factorization approach for efficiency. As discussed in Sec. 2, a matrix-free tensor-product preconditioner based on approximate factorization of the inviscid operator is used, and performs well in convection-dominated regions of the flow, which is the majority of the flowfield for external aerodynamics applications. A numerical test sets the source term $S = 0$ in Eqn. 3, and modifies the diffusion coefficient to examine the convergence of the nonlinear system (*cf.* Fig. 5). As expected, our current preconditioner fares very poorly
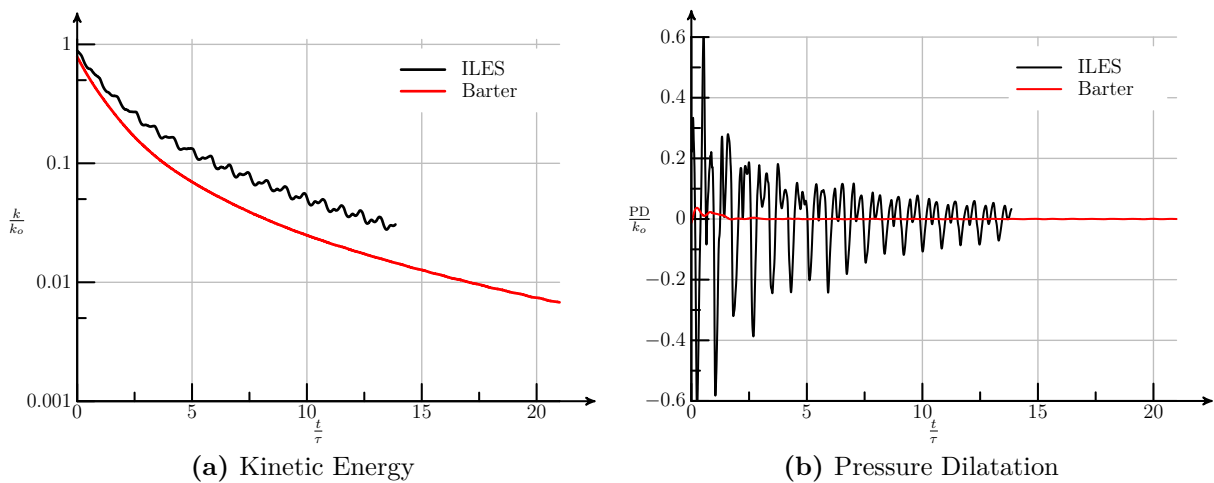
American Institute of Aeronautics and Astronautics

(a) Kinetic Energy

(b) Pressure Dilatation

Figure 4: Evolution of turbulence for homogeneous isotropic turbulence. k_o is the target initial kinetic energy and τ is the eddy turnover time. ($Re_\lambda = 45$, $Ma_t = 0.6$)
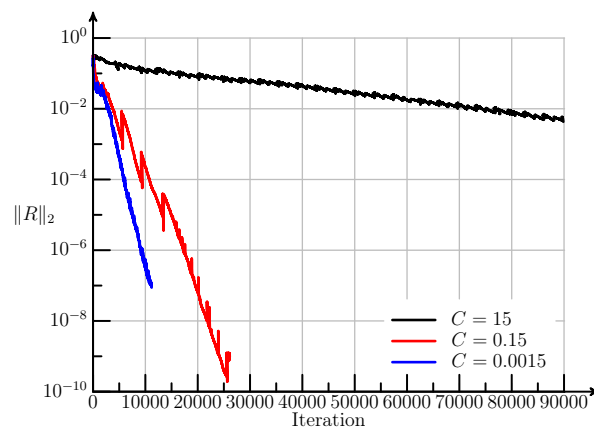

Figure 5: Convergence for the RAE 2822 airfoil simulation using varying artificial viscosity dissipation coefficients and $S = 0$.

converging this system when the auxiliary equation is dominated by diffusion.

6 Modified Artificial Viscosity

Attempts were made to modify the original Barter and Darmofal differential equation to improve the predictive ability and numerical properties to little effect. While modifying the preconditioner is certainly possible, current options would require too much computational expense to be competitive with the existing approach for the scale-resolving simulations of interest. In other words, we prefer to modify the shock-capturing scheme to suit the

characteristics of the solver, rather than *vice versa*. Further, the source term, which drives the behavior of the artificial viscosity, contains an imposed temporal scale. In turbulent simulations there is a broad range of scales of interest, and focusing the response of the shock sensor to a single scale is problematic. For these reasons, we examine a scheme which does not require an auxiliary differential equation to drive the artificial viscosity, but maintains the same jump shock sensor (Eqn. 5). The main motivations proposed for constructing a smooth artificial viscosity using a Poisson equation are improved robustness and accuracy. This section will provide a preliminary assessment of these rationale for the current DGSEM solver.

6.1   Numerical Test Cases

The stiffness of Barter and Darmofal's model precludes the current DGSEM solver converging on standard test cases for shock capturing. Beyond verification cases, only unsteady simulations such as provided above were possible, and even these are computationally prohibitive. Given this, a detailed comparison of the current modified artificial viscosity model against similar results from Barter and Darmofal's is not possible. Instead, the performance of the modified shock-capturing scheme is evaluated on four representative configurations described here. The first two cases are steady transonic ($M_\infty = 0.9$) and supersonic ($M_\infty = 1.2$) viscous flow over a NACA 0012 airfoil at 5° angle of attack and a Reynolds number of 60,000. The transonic case produces relatively weak shocks, but still strong enough that the current fluid solver becomes unstable at high order without some form of augmentation. The supersonic case produces a weak bow shock and pair of fish-tail shocks aft of the trailing edge. Both airfoil configurations involve interactions between the shock and a viscous shear layer.

The third test case is a more challenging steady, inviscid supersonic ($M_\infty = 4$) blunt body configuration developed for the International Workshop on High Order CFD Methods (HOW)[24]. This case has simple well-defined boundary conditions, along with analytic error measures for total enthalpy and stagnation pressure loss, that allow for comparison against current state-of-the-art finite-difference and finite-volume methods.

The final test case is decay of homogeneous isotropic turbulence (HIT) at an initially high turbulent mach number described above in Sec. 5.

All of the computational cases are intentionally tested using relatively coarse resolutions as this is the most challenging situation for the shock-capturing scheme. Further, the NACA 0012 airfoil cases use a "generic" mesh that is not adapted to the shock locations in any way. The supersonic bow shock configuration does use shock-adapted grids for consistency

with the HOW test case. The element boundaries for the two baseline computational mesh are presented in Fig. 6. Isolated cases are tested in refinement to demonstrate properties of the schemes with increasing resolution. All of the test cases presented herein converge to machine epsilon, either for a steady-state simulation, or for every step of an unsteady simulation.
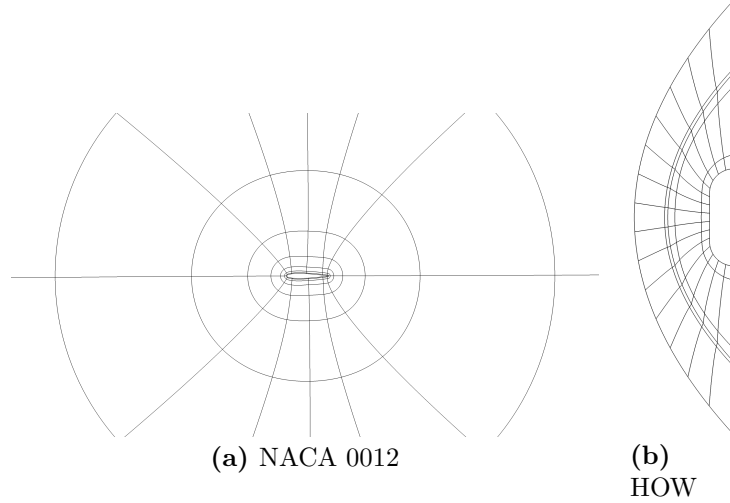

(a) NACA 0012   **(b)** HOW

Figure 6: Element boundaries for the numerical experiments computational mesh.

6.2 Formulation

To begin, the working variable for the artificial viscosity is interpreted as the inverse of a local element Reynolds number,

$$\epsilon^{-1} = Re_h = \frac{\rho \lambda \bar{h}}{\mu_s} \tag{8}$$

where $\lambda = \sqrt{u_k u_k}$ is a local velocity scale, not a spectral radius approximation of the flux Jacobian, and $\bar{h} = \frac{\mathcal{V}^{1/3}}{p+1}$ is a local length scale. When $\epsilon \downarrow 0, Re_h \uparrow \infty, \mu_S \downarrow 0$ and the shock-capturing viscosity is negligible. Near discontinuities $\epsilon \uparrow 1, Re_h \downarrow 1, \mu_S \uparrow \rho \lambda \bar{h}$.

Ducros *et al.* [25] devised a sensor which automatically distinguishes regions of significant vorticity from regions of significant dilatation. A modified version of this sensor, which also responds to regions of pure shear, is used in the current work,

$$d = \frac{2u_{j,j}u_{k,k}}{u_{j,j}u_{k,k} + u_{i,j}u_{i,j} + \epsilon_d} \tag{9}$$

American Institute of Aeronautics and Astronautics

where ϵ_d is a scalar near machine epsilon that filters the ratio when numerator and denominator are both negligible.

Figure 7a presents the variation of the modified Ducros sensor for the flow over the supersonic NACA 0012 test case at 8th-order. While the sensor reliably recognizes the region of the bow shock and the boundary layer, in the majority of the domain the sensor displays a highly oscillatory behavior that counteracts the efficacy of the sensor. This is caused by the gradients being represented by high-order polynomials, then squared and formed into a ratio, *i.e.* it is simply a consequence of the nature of a high-order representation.

To ameliorate this problem we utilize the modified sensor in a volume-averaged sense,

$$\bar{d} = \frac{\int d\left(x_i\right) d\mathcal{V}}{\int d\mathcal{V}} \tag{10}$$

Figure 7b presents the volume-averaged modified Ducros sensor for the same supersonic NACA 0012 test case as Fig. 7a. Utilized in this manner the sensor reliably targets elements which are dilatation dominated $(\bar{d} \to 1)$ from those that are shear dominated $(\bar{d} \to 0)$.
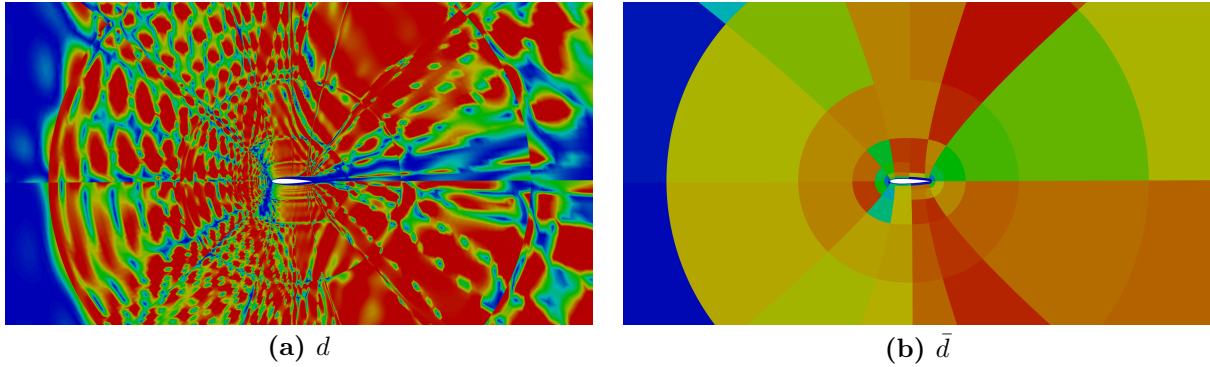

(a) d **(b)** $\bar{d}$

Figure 7: Behavior of the modified Ducros sensor, Eqns. 9 and 10, for the flow over a NACA 0012 ($Ma = 1.2$, $\alpha = 5°$, $Re = 60$k).

The artificial viscosity Reynolds number is then formed using the jump sensor, Eqn. 5. As with the original model, the exponential variation of the sensor is used to control the behavior of the artificial viscosity. The functional form is given by

$$\psi = \log_{10}\left(\bar{d}J_\kappa\right) + 1 \tag{11}$$

$$\epsilon = Re_h^{-1} = \frac{1}{2}\left[1 + \tanh\left(2\psi\right)\right] \tag{12}$$

This rapidly turns the sensor on when $\bar{d}J_\kappa$ exceeds 10^{-1}. This intentionally provides a

relatively modest amount of artificial viscosity. For comparison, Barter and Darmofals' original model turned on when the sensor exceeded roughly 10^{-3}, and the sensor was not modified by the Ducros' sensor. Here the entropy-stable scheme in inherently dissipative, and it is observed to remain stable at higher speeds when traditional schemes based on conservative variables diverge (*cf.* [26]), thus we expect to require less artificial viscosity more sharply focused near discontinuities. As discussed in Sec. 4, we construct an artificial shear viscosity and satisfy Stokes' hypothesis, as this is empirically more stable in the current scheme. This artificial viscosity scheme retains the entropy-stability property.

Equation 11 is not the only method to incorporate the Ducros-style sensor into the artificial viscosity formulation, but does provide a baseline formulation. Other methods may be tested going forward.

The variation of Mach number and artificial viscosity for the simulation of a NACA 0012 at $Ma = 0.9$, $\alpha = 5°$ is presented in Fig. 8 for 2nd-, 4th-, and 8th-order simulations on a coarse mesh with 96 elements. As expected, the quality of the solution at this resolution is poor, and the artificial viscosity is clearly discontinuous between elements, however the simulations all remain stable and converge to machine epsilon. As the resolution is increased with increasing order, the resolution of the shock, boundary layer, and wake improves, and the the artificial viscosity responds to the new location and strength. Elements which share a face crossed by the shock both see increased viscosity, however the local geometric scaling ($\bar{h}$) greatly increases the artificial viscosity as the mesh coarsens. Unlike the Barter and Darmofal model there is no artificial viscosity produced in the expansion region around the leading edge.

For completeness, a refined mesh simulation at 8th-order is performed for the NACA 0012 transonic test case (Fig. 10). With the improved resolution the flow structure and the boundary layer are dramatically changed. A weak shock upstream on the airfoil surface thickens the boundary layer and a weak shock forms in the wake structure. The maximum artificial viscosity is reduced by an order of magnitude, as desired, and is localized around the wake shock structures. The goal of the current artificial viscosity scheme is to maintain stability on a coarse mesh so that (ultimately) an $h - p$ adaptation strategy can refine the mesh appropriately, however coarse resolution of shocks is still necessary in a refined limit, as many regions of the flow may not contribute substantially to an output functional and hence should not command significant computational resources.

Similar to the previous results, the variation of Mach number and artificial viscosity for the simulation of a NACA 0012 at $Ma = 1.2$, $\alpha = 5°$ is presented in Fig. 9 using spectral re-

American Institute of Aeronautics and Astronautics

(a) Mach number

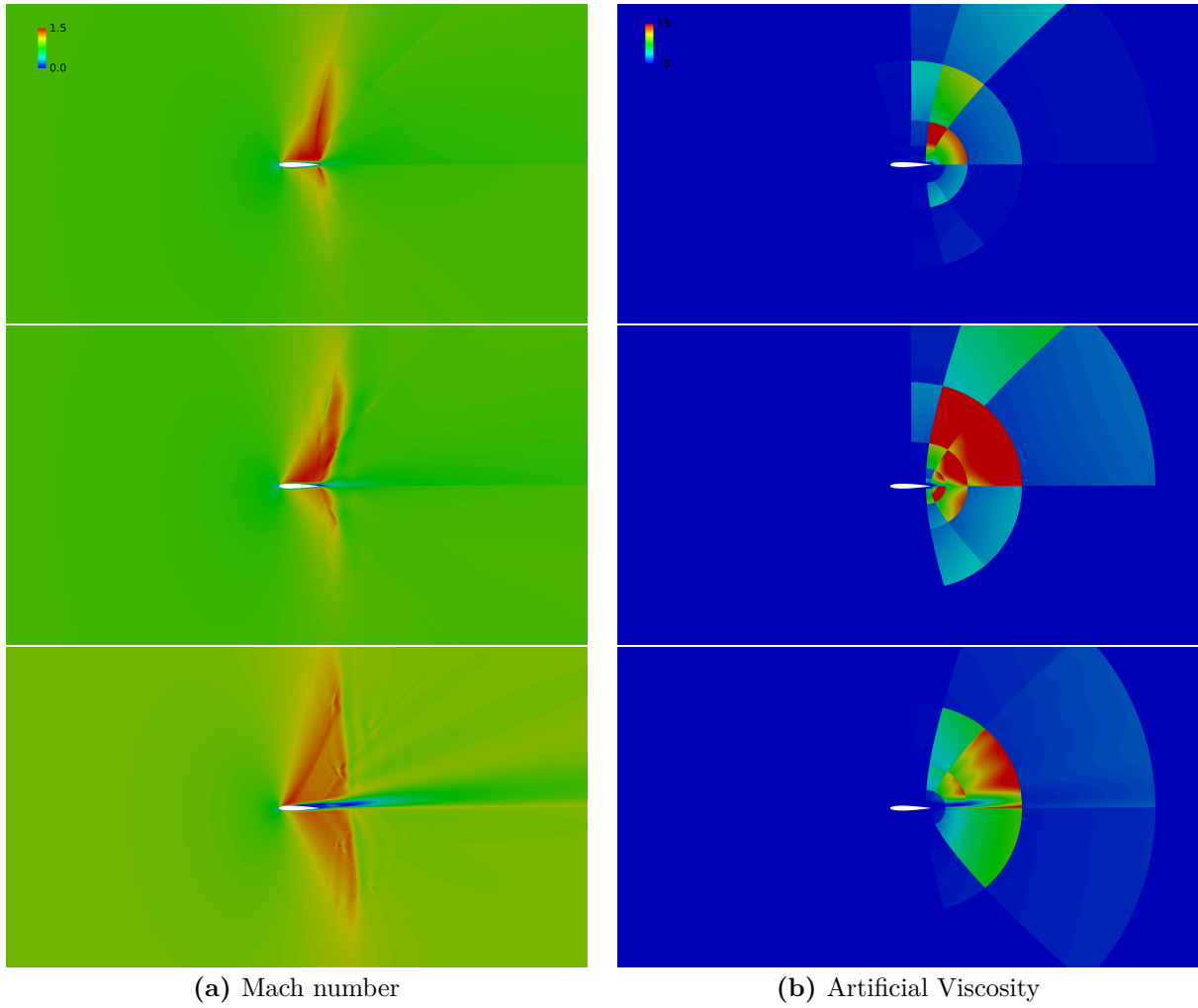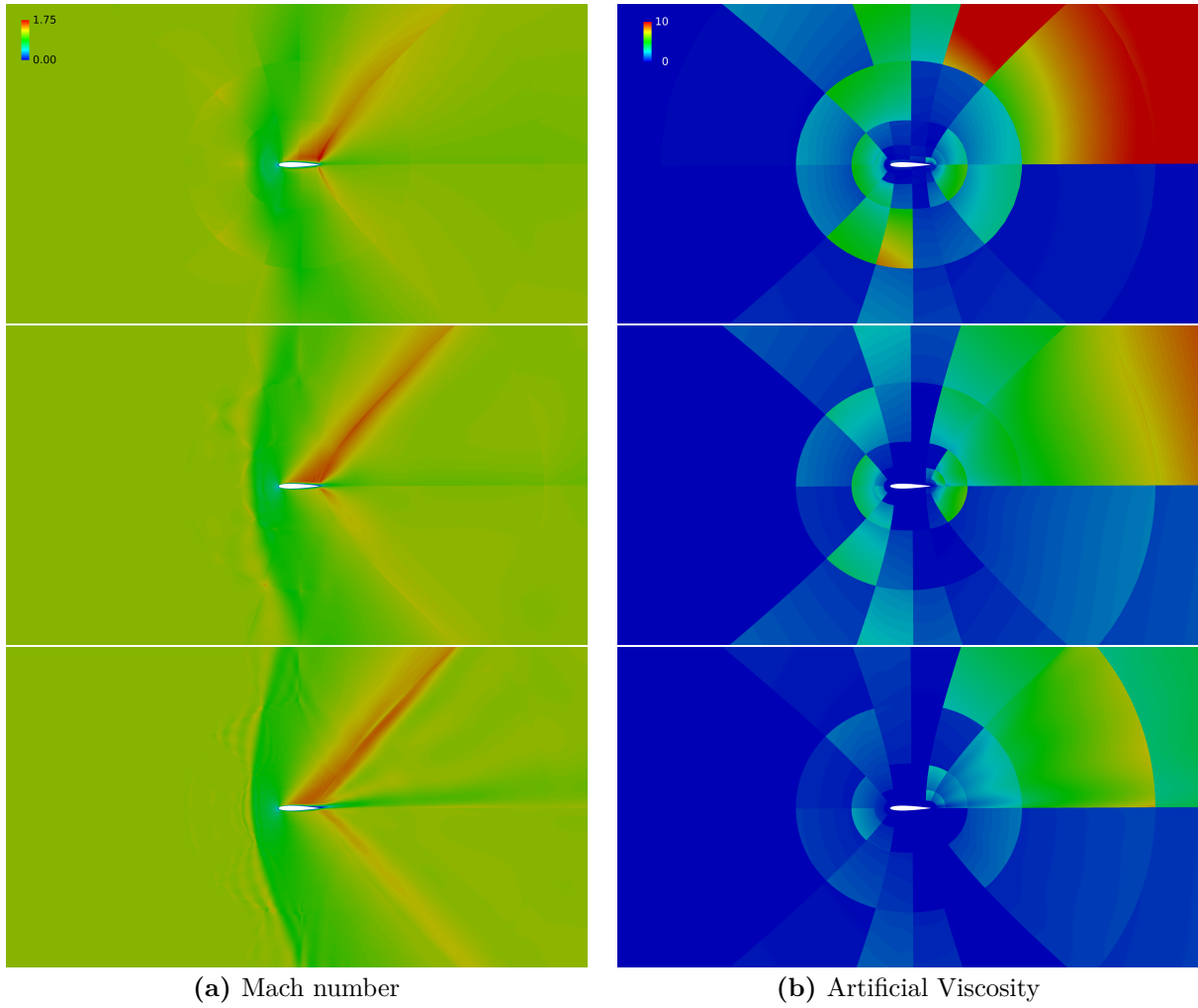**(b)** Artificial Viscosity

Figure 8: Computed results for the flow over a NACA 0012. The top row contains 2nd-order simulations, the middle row 4th-order, and the bottom row 8th-order. ($Ma = 0.9$, $\alpha = 5°$, $Re = 60$k).

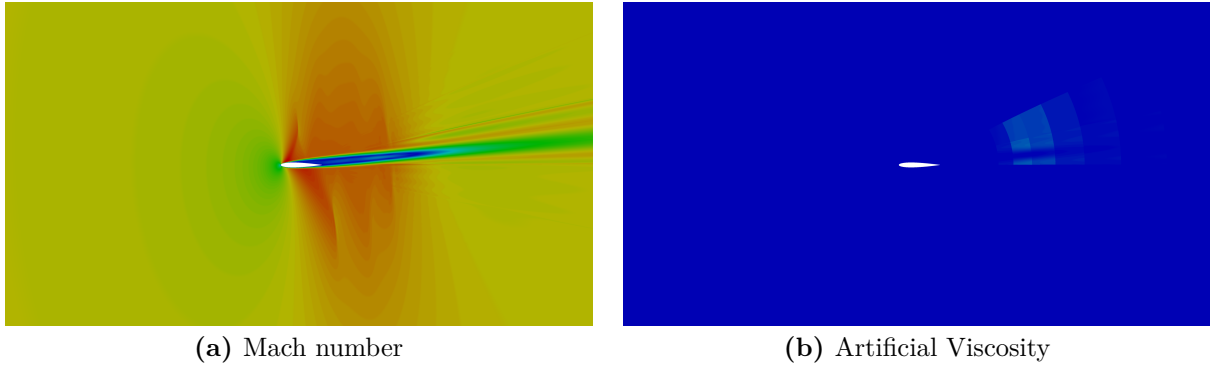**(a)** Mach number

(b) Artificial Viscosity

Figure 9: Computed results for the flow over a NACA 0012. The top row contains 2nd-order simulations, the middle row 4th-order, and the bottom row 8th-order. ($Ma = 1.2$, $\alpha = 5°$, $Re = 60$k).

American Institute of Aeronautics and Astronautics

(a) Mach number

(b) Artificial Viscosity

Figure 10: Computed results for the flow over a NACA 0012 on a refined mesh ($Ma = 0.9$, $\alpha = 5°$, $Re = 60$k).
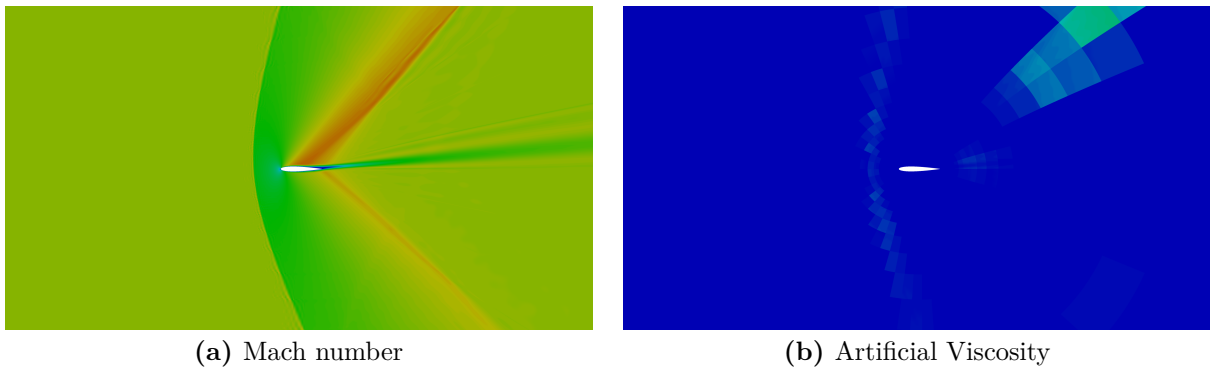

(a) Mach number

(b) Artificial Viscosity

Figure 11: Computed results for the flow over a NACA 0012 on a refined mesh ($Ma = 1.2$, $\alpha = 5°$, $Re = 60$k).

American Institute of Aeronautics and Astronautics

finement on the same coarse mesh. Again, the resolution of the flowfield in these simulations is relatively poor, however the simulations remain stable and converge to machine epsilon. The artificial viscosity does reduce as the resolution is increased, as desired. A refined mesh simulation at 8th-order is presented in Fig. 11. As desired, the qualitative behavior of the simulation is greatly improved with the increased resolution and the maximum artificial viscosity is reduced by an order of magnitude and either localized to the bow shock region or present in coarse elements away from the body.

The computed results for the supersonic blunt body flow are presented next in Fig. 12. For this configuration the 8th-order simulation remains stable, but does not converge to machine epsilon, and hence is not included. The artificial viscosity is not normalized for this inviscid simulation. For this case a feature-aligned grid is utilized and the qualitative nature of the simulation is improved greatly, and there are no obvious artifacts due to the discontinuous nature of the artificial viscosity.

The error in total enthalpy in the domain is computed and compared against similar results using 2nd-order schemes from the OVERFLOW solver[27] using similar grids in Fig. 13. The current results are on par with the reference results. Lastly, slices of pressure through the simulated flowfield along the stagnation line and the surface are presented in Fig. 14. Along the stagnation streamline the Gibbs phenomena is largely suppressed at both N=2 and N=4. Considering the pressure variation along the surface, with this coarse resolution the element boundaries are evident at 2nd order, but the jump is greatly reduced at 4th order, and the pressure remains smooth everywhere despite the discontinuous artificial viscosity field. The surface stagnation pressure for both simulations agrees well with the Rayleigh-pitot formula ($\frac{p}{\rho_{ref}a_{ref}^2} = 15.0486$).

Lastly, the decaying homogeneous turbulence computed earlier using Barter and Darmofal's scheme is reproduced (Figs. 15 and 16). The maximum artificial viscosity is roughly 2 orders of magnitude lower using the current modified scheme, and in many regions of the flow becomes negligible, as desired. The decay of kinetic energy and pressure dilatation is very close to the reference simulation, indicating the artificial viscosity is providing some localized stabilization, but not damping the turbulence significantly. The computational cost with the new approach is equivalent to the baseline implicit LES simulation.
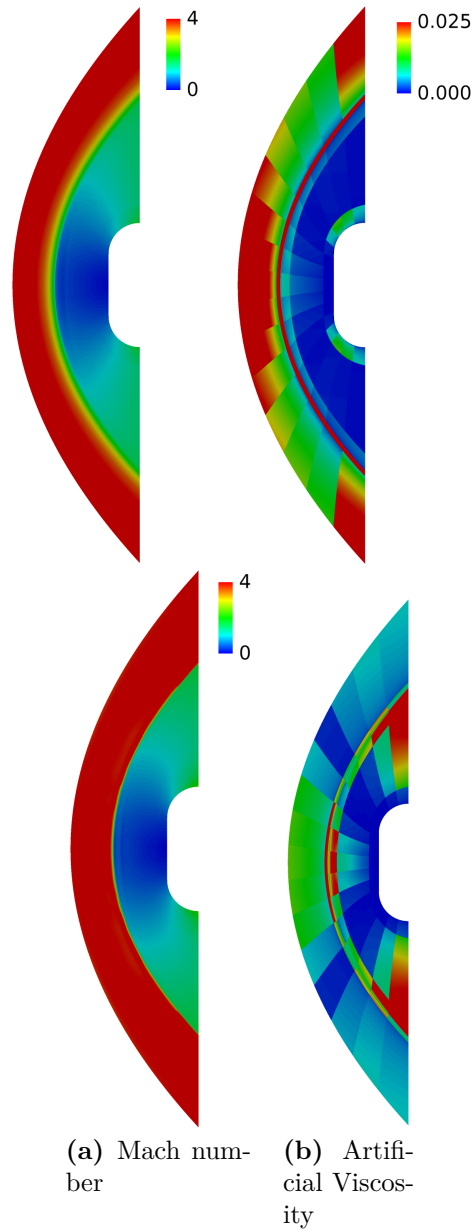
(a) Mach number

(b) Artificial Viscosity

Figure 12: Computed results for the flow over the HOW supersonic blunt body. The top row contains 2nd-order simulations and the middle row 4th-order. $(Ma = 4)$.
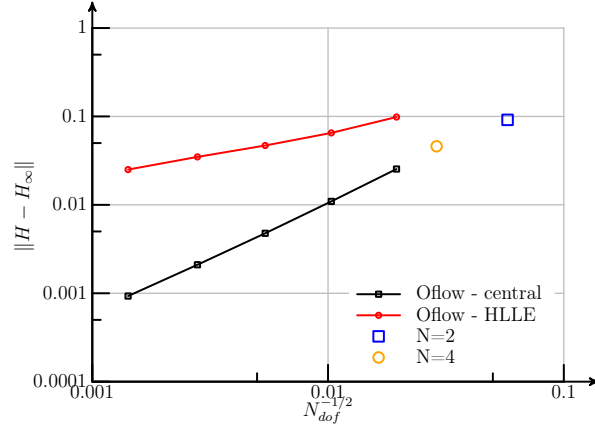
American Institute of Aeronautics and Astronautics

Figure 13: Computed error in total enthalpy for the HOW supersonic blunt body ($Ma = 4$).
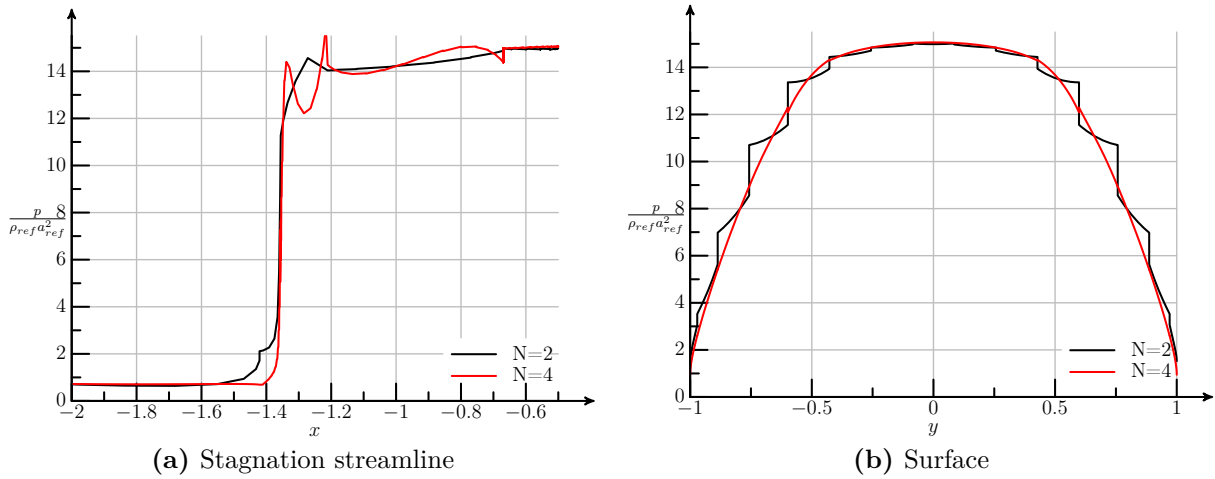

(a) Stagnation streamline

(b) Surface

Figure 14: Distribution of pressure along selected lines for the flow over the HOW supersonic blunt body ($Ma = 4$).

(a) Mach number

(b) Artificial Viscosity

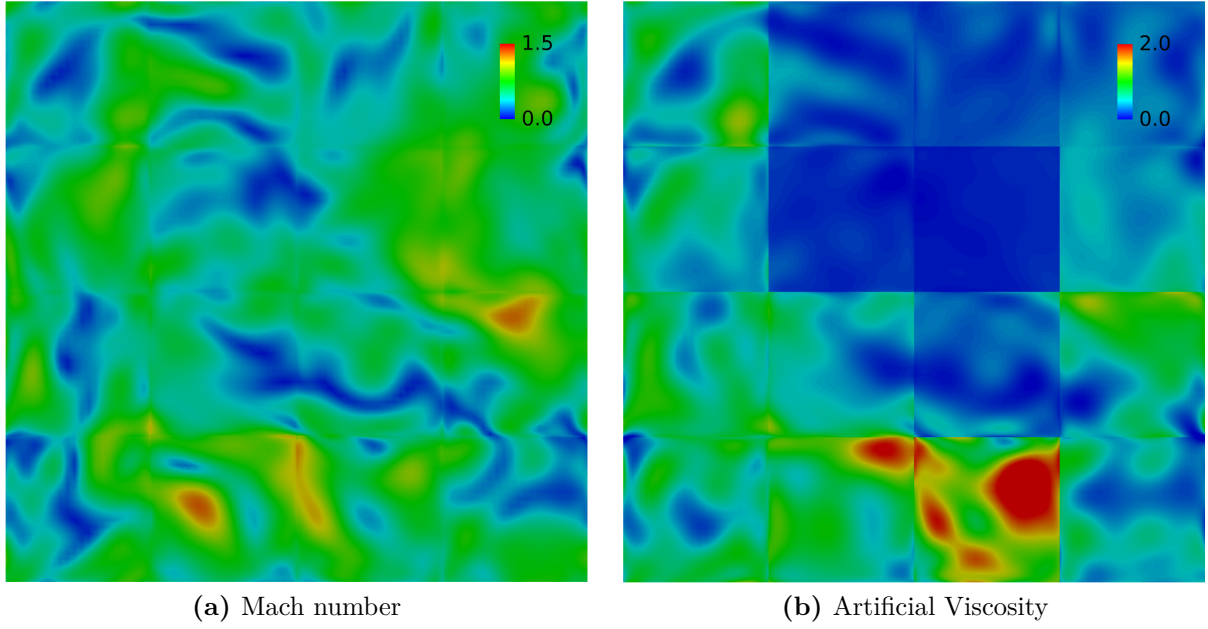**Figure 15:** A snapshot through the domain during the decay of homogeneous isotropic turbulence ($Re_\lambda = 45$, $Ma_t = 0.6$).

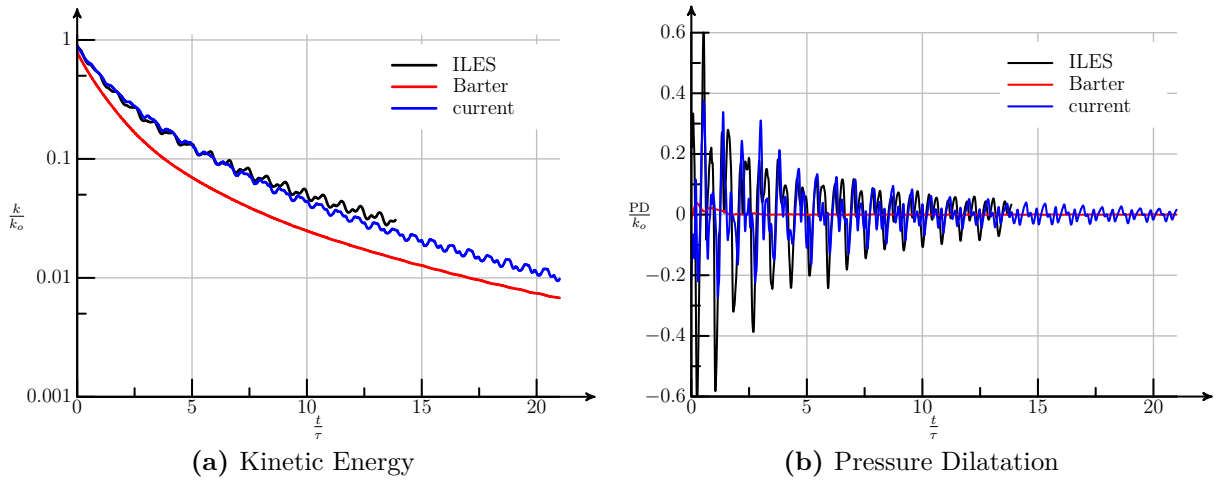**(a)** Kinetic Energy

(b) Pressure Dilatation

Figure 16: Evolution of turbulence for homogeneous isotropic turbulence. k_o is the target initial kinetic energy and τ is the eddy turnover time. ($Re_\lambda = 45$, $Ma_t = 0.6$)

7 Review

An *ad-hoc* artificial-viscosity formulation for shock capturing is designed for a DGSEM solver for scale-resolving simulations. The primary emphasis to-date has been on the robustness of the scheme at relatively coarse resolution, as this is the most challenging use case for shock-capturing. The initial results are encouraging, and a relatively simplistic scheme successfully converges transonic and supersonic benchmark problems, while not destroying turbulence features in tests of HIT. Despite the discontinuous nature of the artificial-viscosity field, the simulation results remain smooth. Further study of accuracy requires inclusion of $h - p$ adaptation and feature-aligned meshing for comparison.

The current results indicate that a smooth artificial-viscosity field is not a strict requirement for robustness or smoothness of the resulting fluid fields. Examining Fig. 1b and Fig. 7a it may be that smoothing formulations are successful by filtering highly oscillatory constructions that are a natural consequence of a high-order representation, rather than enforcing a C^p-continuous artificial-viscosity field. The current approach of agglomerating sensors within an element achieves the same goal in a different manner.

References

[1] L. Diosady and S. Murman, "Design of a Variational Multiscale Method for Turbulent Compressible Flows," AIAA Paper 2013-2870, June 2013.

[2] L. Diosady and S. Murman, "Higher-Order Methods for Compressible Turbulent Flows Using Entropy Variables," AIAA Paper 2105-0294, 2015.

[3] Diosady, L.T. and Murman, S.M., "General element shapes within a tensor-product higher-order space-time discontinuous-Galerkin formulation," AIAA Paper 2015-3044, 2015.

[4] Garai, A., Diosady, L.T., Murman, S.M., and Madavan, N., "DNS of Flow in a Low-Pressure Turbine Cascade Using a Discontinuous-Galerkin Spectral-Element Method," in *Proceedings of ASME Turbo Expo 2015*, no. GT2015-42773, 2015.

[5] Murman, S.M., Diosady, L.T., Garai, A., and Ceze, M., "A Space-Time Discontinuous-Galerkin Approach for Separated Flows," AIAA Paper 2016-1059, 2016.

[6] Garai, A., Diosady, L.T., Murman, S.M., and Madavan, N., "DNS of Flow in a Low-Pressure Turbine Cascade with Elevated Inflow Turbulence Using a Discontinuous-Galerkin Spectral-Element Method," in *Proceedings of ASME Turbo Expo 2016*, no. GT2016-56700, 2016.

[7] C. E. Baumann and J. T. Oden, "A discontinuous hp finite element method for the Euler and Navier–Stokes equations," *International Journal for Numerical Methods in Fluids*, vol. 31, no. 1, pp. 79–95, 1999.

[8] A. Burbeau, P. Sagaut, and C.-H. Bruneau, "A Problem-Independent Limiter for High-Order Runge–Kutta Discontinuous Galerkin Method," *Journal of Computational Physics*, vol. 169, pp. 111–150, may 2001.

[9] P.-O. Persson, "Shock capturing for high-order discontinuous galerkin simulation of transient flow problems," AIAA Paper 2013-3061, jun 2013.

[10] Y. Lv, Y. C. See, and M. Ihme, "A general and robust high-order numerical framework for shock-capturing: entropy-bounding, shock detection and artificial viscosity," AIAA Paper 2015-0572, jan 2015.

[11] G. E. Barter and D. L. Darmofal, "Shock capturing with PDE-based artificial viscosity for DGFEM: Part I. Formulation," *Journal of Computational Physics*, vol. 229, pp. 1810–1827, mar 2010.

[12] J. Reisner, J. Serencsa, and S. Shkoller, "A space–time smooth artificial viscosity method for nonlinear conservation laws," *Journal of Computational Physics*, vol. 235, pp. 912–933, feb 2013.

[13] N. K. Burgess and D. J. Mavriplis, "Computing shocked flows using a discontinuous galerkin method," AIAA Paper 2012-2715, 2012.

[14] Brazell, M. and Mavriplis, D.J., "3D Mixed Element Discontinuous Galerking with Shock Capturing," AIAA Paper 2013-3064, 2013.

[15] Galeão, A.C. and Dutra Do Carmo, E.G., "A Consistent Approximate Upwind Petrov-Galerkin Method for Convection-dominated Problems," *Computer Methods in Applied Mechanics and Engineering*, vol. 68, pp. 83–95, 1988.

[16] T. J. Barth, "Numerical methods for gasdynamic systems on unstructured meshes," in *An Introduction to Recent Developments in Theory and Numerics for Conservation Laws* (D. Kroner, M. Olhberger, and C. Rohde, eds.), pp. 195–282, Springer Verlag, Berlin, 1999.

[17] Hiltebrand, A. and Mishra, S., "Entropy Stable Shock Capturing Space-time Discontinuous Galerkin Schemes for Systems of Conservation Laws," Research Report 2012-07, Swiss Federal Institute of Technology Zurich, 2012.

[18] Ismail, F. and Roe, P.L., "Affordable, Entropy-consistent Euler flux functions II: entropy production at shocks," *Journal of Computational Physics*, vol. 228, no. 15, pp. 5410–5436, 2009.

[19] Bassi, F. and Rebay, S., "A high-order accurate discontinuous finite element method foro the numerical solution of the compressible Navier-Stokes equations," *Journal of Computational Physics*, vol. 131, no. 2, pp. 267–279, 1997.

[20] Diosady, L.T. and Murman, S.M., "Tensor-Product Preconditioners for Higher-Order Space-Time Discontinuous Galerkin Methods," *Journal of Computational Physics*, vol. 330, no. 1, pp. 296–318, 2017.

[21] A. Mani, J. Larsson, and P. Moin, "Suitability of artificial bulk viscosity for large-eddy simulation of turbulent flows with shocks," *Journal of Computational Physics*, vol. 228, no. 19, pp. 7368 – 7374, 2009.

[22] Dulikravich, G.S., "Stokes' hypothesis and entropy variation within a compression shock," in *23rd International Symposium on Shock Waves*, 2001.

[23] L. Krivodonova, J. Xin, J.-F. Remacle, N. Chevaugeon, and J. Flaherty, "Shock detection and limiting with discontinuous galerkin methods for hyperbolic conservation laws," *Applied Numerical Mathematics*, vol. 48, no. 3, pp. 323 – 338, 2004.

[24] "5th International Workshop on High-Order CFD Methods." `https://how5.cenaero.be`.

[25] F. Ducros, V. Ferrand, F. Nicoud, C. Weber, D. Darracq, C. Gacherieu, and T. Poinsot, "Large-eddy simulation of the shock/turbulence interaction," *Journal of Computational Physics*, vol. 152, no. 2, pp. 517 – 549, 1999.

American Institute of Aeronautics and Astronautics

[26] Hillewaert, K., Cagnone, J.S., Murman, S.M., Garai, A., Lv, Y., and Ihme, M., "Assessment of high-order DG methods for LES of compressible flow," in *Center for Turbulence Research Proceedings of the Summer Program 2016*, September 2016.

[27] Nichols, R.H., Tramel, R.W., and Buning, P.G., "Solver and Turbulence Model Upgrades to OVERFLOW 2 for Unsteady and High-Speed Applications," AIAA Paper 2006-2824, 2006.

American Institute of Aeronautics and Astronautics